

Article

# Multi-Objective Optimization for Outer Rotor Low-Speed Permanent Magnet Motor

Guanghui Du <sup>\*</sup>, Chengshuai Hu, Qixun Zhou, Wentao Gao and Qizheng Zhang

School of Electrical and Control Engineering, Xi'an University of Science and Technology, Xi'an 710054, China

<sup>\*</sup> Correspondence: [duguanghui1104@163.com](mailto:duguanghui1104@163.com)

**Abstract:** For outer rotor low-speed permanent magnet motors (LSPMMs), in the optimization design process, not only is the electromagnetic performance optimized, but the influence of the thermal load and copper loss on the temperature in the electromagnetic parameters should also be considered. However, these optimized designs that comprehensively consider electromagnetic performance and temperature characteristics are rare in the existing literature. Therefore, this paper focuses on a multi-objective optimization process considering efficiency, thermal load and copper loss. Firstly, according to the initial design, the influence of the design parameters on the efficiency and thermal load is analyzed, and the range of optimization parameters is determined. Next, the response surface is built, the response-surface analysis of electromagnetic performance is performed, and the parameter sensitivity is calculated. Then, the multi-objective optimization design is carried out by comprehensively considering the electromagnetic performance and temperature. Finally, compared with the initial scheme, the optimized scheme improves the efficiency and reduces the temperature, and the optimized scheme is verified by experimentation on a 22 kW, 56 rpm LSPMM prototype, which can provide a reference for the multi-objective optimization of LSPMMs by comprehensively considering the electromagnetic performance and temperature.



**Citation:** Du, G.; Hu, C.; Zhou, Q.; Gao, W.; Zhang, Q. Multi-Objective Optimization for Outer Rotor Low-Speed Permanent Magnet Motor. *Appl. Sci.* **2022**, *12*, 8113. <https://doi.org/10.3390/app12168113>

Academic Editors: Gang Lei, Jianguo Zhu, Youguang Guo and Yujiao Zhang

Received: 25 July 2022

Accepted: 11 August 2022

Published: 13 August 2022

**Publisher's Note:** MDPI stays neutral with regard to jurisdictional claims in published maps and institutional affiliations.



**Copyright:** © 2022 by the authors. Licensee MDPI, Basel, Switzerland. This article is an open access article distributed under the terms and conditions of the Creative Commons Attribution (CC BY) license (<https://creativecommons.org/licenses/by/4.0/>).

**Keywords:** low-speed permanent magnet motor; outer rotor; sensitivity analysis; multi-objective optimization; efficiency; temperature

## 1. Introduction

Outer rotor low-speed permanent magnet motors (LSPMMs) have extremely wide application prospects in the fields of industrial production, coal mine development, port lifting and ship propulsion [1–3]. The low-speed permanent magnet synchronous motor studied in this paper can be applied to the coal mine belt conveyor, replacing the traditional method of driving the asynchronous motor and the reducer used in the coal mine. For the LSPMM, it is usually run at the rated speed and rated torque point, that is, mainly at the rated load point. In the application of the coal mine belt conveyor, the LSPMM has a higher efficiency and a higher power factor than the induction motor, and the LSPMM can maintain good performance in a wide range of load changes [4]. In addition, compared with the inner rotor motor, the outer rotor LSPMM has a larger moment of inertia, less copper loss, a higher output power, a stronger power density, and the outer rotor LSPMM is more convenient to be made into a multi-level structure [5,6]. For the LSPMM, electromagnetic performance is a very important performance index, which can reduce the motor long-term operating costs and result in a longer working life [7]. Temperature is also an important evaluation criterion for the LSPMM. If the temperature is too high, it will not only affect the safety of operation, but also reduce the motor service life. An excessive winding temperature may harm the insulation of the motor [8], and an excessive PM temperature will cause irreversible demagnetization of the PM [9]. Loss is an important factor affecting the motor temperature; the heat generated by various losses can significantly increase the temperature of the motor, and even when the total losses are the same, the different

proportions of losses will have a large impact on the motor temperature [10]. For the LSPMM, the stator winding copper loss accounts for the vast majority of the total loss, and the effect of copper loss on the motor maximum temperature is also the largest compared to other losses [11]. Therefore, when optimizing the motor, it is not only necessary to pursue excellent electromagnetic performance, but also to consider the influence of thermal load parameters on the temperature in electromagnetic performance.

In the existing literature, the electromagnetic performance and temperature of the LSPMM have been optimized based on some multi-objective optimization methods. For the efficiency performance, five different rotor topologies (V-shape, U-shape, double V-shape, delta-shape, and double tangential-shape) were optimized by the particle swarm optimization (MPSO) algorithm, and their performance characteristics such as efficiency and anti-demagnetization ability were compared [12]. For the power density, the differential evolution algorithm was used to optimize the motor parameters in order to pursue a high power density, including the stator yoke thickness, the rotor yoke thickness and the motor relative magnet span [13]. For the torque performance, a new flux-assisted consequent pole spoke-type permanent magnet (PM) synchronous torque motor was proposed and the rotor design was optimized; the optimized motor had a higher torque-to-magnet-weight ratio and a wider constant power region. [14]. For the temperature characteristics, the motor was optimized for copper loss minimization in pursuit of a low temperature rise [15]. It can be seen that both the electromagnetic performance and temperature are very important for the optimal LSPMM design. For the LSPMM, electromagnetic performance is an important performance index, including the power factor, back EMF, torque density, etc. Optimizing the electromagnetic performance can greatly improve the motor working efficiency and reduce the motor cost, but the highest electromagnetic performance may lead to an increase in the motor temperature and reduce the motor working life [16]. The temperature also has a great influence on the motor. A lower temperature can prolong the motor service life and reduce the motor noise; however, in the optimization process, only considering the temperature optimization may reduce the electromagnetic performance [17]. It can be seen from the above description that neither the electromagnetic performance nor the temperature of the motor is ignored. In the existing literature, the electromagnetic performance is usually designed and optimized for the highest efficiency, without considering the influence of the electromagnetic parameters on the motor temperature. These optimizations can achieve high efficiency, but may result in high motor temperatures due to different loss distributions and large thermal loads. Therefore, in this paper, in order to fully optimize the electromagnetic performance and temperature characteristics of the LSPMM, the multi-objective optimization of the motor is carried out considering the electromagnetic performance and temperature characteristics.

In this paper, in order to consider the effects of the design parameters on the electromagnetic performance and temperature performance, a multi-objective optimization is carried out based on the consideration of efficiency, thermal load and copper loss for the LSPMM. Firstly, a sensitivity analysis of the design parameters is performed. Then, the optimization objective is set in order to perform a multi-objective optimization of the motor. Finally, a prototype is made, and the optimization scheme is experimentally verified. Section 2 presents the initial design of the LSPMM. Section 3 begins with the analysis of the optimization parameters for efficiency and thermal load, followed by the response-surface analysis, and calculates the parameter sensitivities. Section 4 performs the multi-objective optimization of the LSPMM based on NSGA-II. In Section 5, the electromagnetic performance and temperature are compared between the initial scheme and the optimized scheme based on finite elements. Section 6 makes a prototype and conducts the experimental verification. Finally, in Section 7, the conclusions drawn are summarized. This paper can provide a reference for the optimal design of the LSPMM by comprehensively considering the electromagnetic performance and temperature.

## 2. Initial Parameters

The structure of the studied 200 kW, 56 rpm LSPMM is shown in Figure 1 in this paper, which consists of 36 slots and 30 poles. The materials of the stator core and rotor core are non-oriented silicon steel lamination. The permanent magnet materials are NdFeB. The initial design parameters of the LSPMM are listed in Table 1.

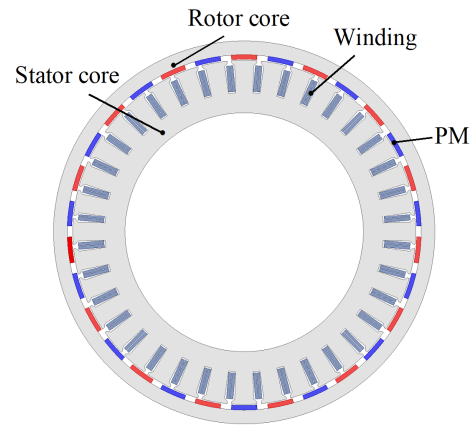


**Figure 1.** Structure of LSPMM.

**Table 1.** Design parameters of the LSPMM.

Parameters	Value
Number of poles	30
Number of stator slots	36
Air gap length (mm)	3
Stator outer diameter (mm)	863
Core length (mm)	930
Pole arc coefficient	0.7
PM thickness (mm)	11
Number of conductors per slot	12

## 3. Comprehensive Sensitivity Analysis

Based on the above analyses, a multi-objective optimization process for the LSPMM is proposed. The detailed multi-objective optimization flowchart is described in Figure 2, which contains the following steps.

Step 1: comprehensive sensitivity analysis. In this step, first an analysis of the influence of single factors on the motor performance parameters is carried out. The single-factor optimization parameters are selected as the pole arc coefficient, PM thickness, stator outer diameter, core length, number of conductors per slot and air gap length, motor performance parameters are efficiency and thermal load. Then, a response-surface analysis of the multi-objective performance is performed. The multi-objective performance parameters are efficiency, no-load back EMF, power factor, core loss, copper loss and thermal load. Finally, based on the Pearson coefficient, the sensitivity of multiple factors to the motor performance parameters is calculated.

Step 2: multi-objective optimization. This step realizes the multi-objective optimization, and generates Pareto front structures in 2D space based on objectives and constraints, and uses NSGA-II to solve the Pareto front and obtain candidate points. Then, the candidate points are compared and the final optimization scheme is determined.

Step 3: performance evaluation. In this step, both the simulation and experiment evaluation are carried out to verify the electromagnetic performances and the temperature rise of the motor, while ensuring the feasibility of a multi-objective optimization scheme.

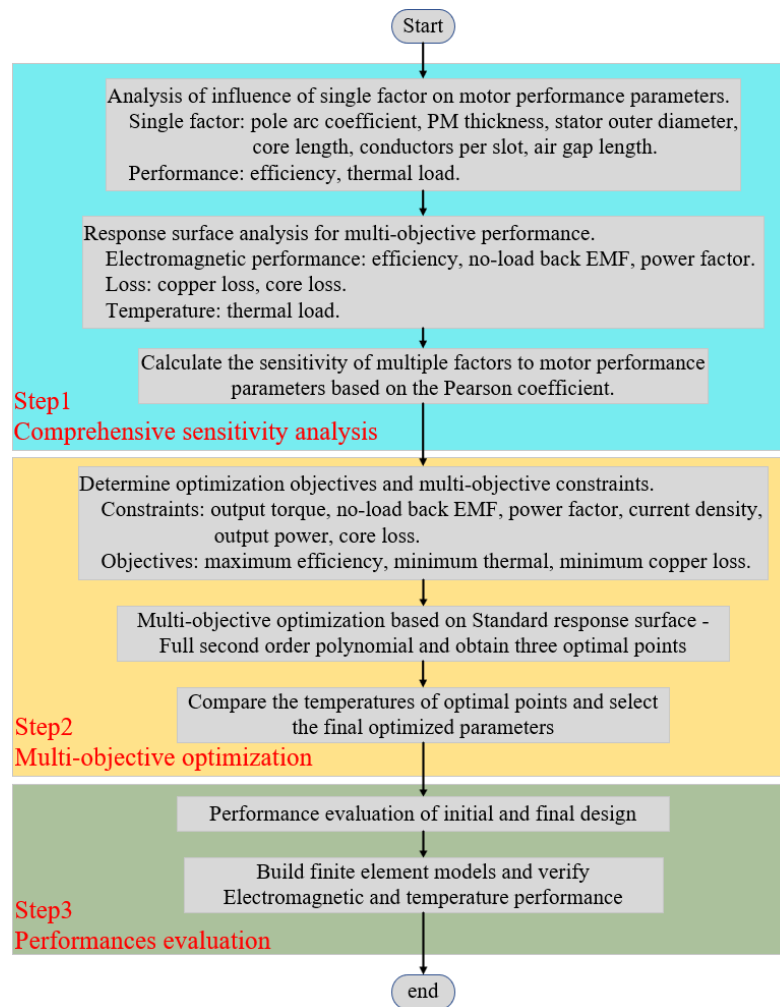


Figure 2. Flowchart of the multi-objective optimization.

### 3.1. Optimization Parameters

In order to obtain a better electromagnetic performance and temperature rise, in the optimization process, six parameters are set as the optimization variables, including the pole arc coefficient, PM thickness, stator outer diameter, core length, number of conductors per slot and air gap length. The influence curves of the single factors on the efficiency and thermal load are shown in Figures 3 and 4.

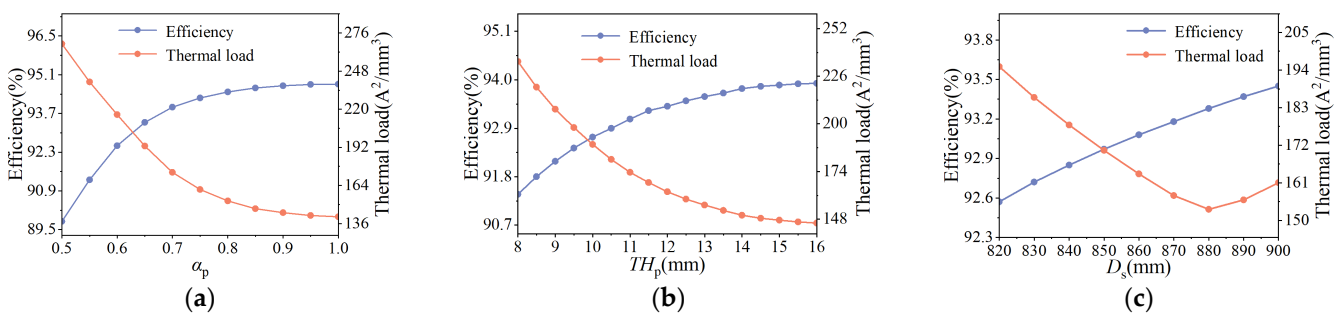
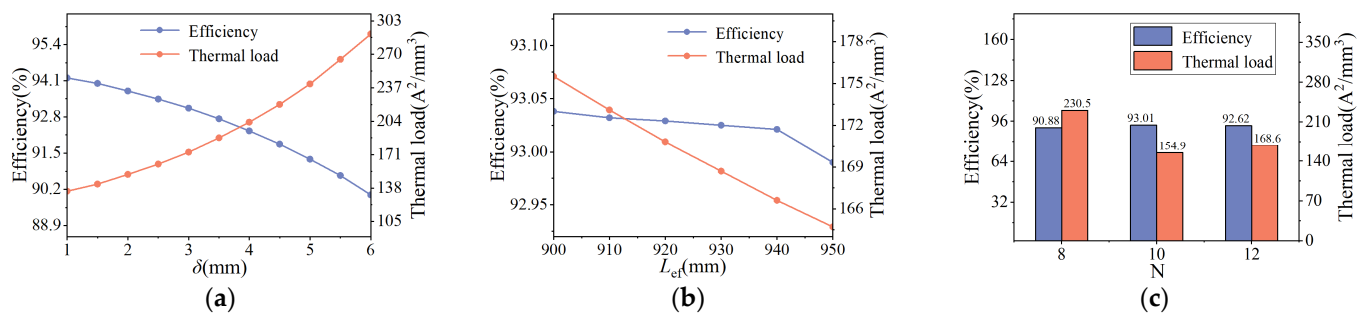


Figure 3. Influence curves of single factors on efficiency and thermal load. (a) Pole arc coefficient; (b) PM thickness; (c) stator outer diameter.



**Figure 4.** Influence curves of single factors on efficiency and thermal load. (a) Air gap length; (b) core length; (c) conductors per slot.

Figure 3 shows the effect of the pole arc coefficient, PM thickness and stator outer diameter on the efficiency and thermal load. In Figure 3a, as the pole arc coefficient increases, the efficiency increases and the thermal load decreases, and when the pole arc coefficient approaches 1, the changes in efficiency and thermal load gradually become stable. Therefore, the variation range of the pole arc coefficient is limited to 0.65–0.95. In Figure 3b, the effect of the PM thickness on the efficiency and thermal load is almost the same as that of the pole arc coefficient. With the increase in PM thickness, the efficiency increases and the thermal load decreases, and both level off. Therefore, the minimum and maximum PM thicknesses are set to 10 mm and 15 mm, respectively. Figure 3c shows the effect of the stator outer diameter on the efficiency and thermal load. As the stator outer diameter increases, the efficiency increases and the thermal load decreases gradually. However, when the stator outer diameter is larger than 880 mm, the thermal load starts to increase again, which is due to the saturation of the iron core when the outer diameter of the stator is too large. Therefore, the optimized range of the stator outer diameter is limited to between 840 mm and 880 mm.

The effect of the air gap length, core length and number of conductors per slot on the efficiency and thermal load are shown in Figure 4. In Figure 4a, with the gradual increase in the air gap length, the efficiency decreases and the thermal load increases, because the long air gap length reduces the air gap magnetic density and the loss increases accordingly. At the same time, considering the assembly of the stator and rotor, the variation range of air gap length is set to 2–5 mm. Figure 4b shows the effect of the core length on the efficiency and thermal load. As the core length increases, both the efficiency and the thermal load decrease. However, when the core length is less than 940 mm, the efficiency decreases slightly with the increase in the core length, and when it is greater than 940 mm, the efficiency begins to decrease greatly. Therefore, the optimized range of the core length is limited to 900–940 mm. In Figure 4c, due to the use of double-layer windings, the number of conductors per slot should only be an even number, so the number of conductors per slot is optimized among 8, 10 and 12. When  $N=8$ , the efficiency is the lowest and the thermal load is the highest, while when  $N=10$ , the electromagnetic performance is better, with the maximum efficiency of 93.01% and the minimum thermal load of 154.9  $A^2/mm^3$ .

After the above analysis, the variation ranges of the six optimized design parameters are listed in Table 2. In the analysis, if the pole arc coefficient is too small, then the efficiency is low and does not meet the requirements. When the pole arc coefficient approaches 1, the efficiency gradually becomes stable and the change is not large. Considering the cost factor, the variation range of the pole arc coefficient is set as 0.65–0.95. In addition, the PM thickness has the same influence characteristics as the pole arc coefficient. If the PM thickness is too small, then it will not meet the magnetic field requirements, and if the PM thickness is too large, then the permanent magnet will be wasted. Therefore, the PM thickness variation range is limited to 10–15 mm. In the optimization, limited by the installation size, the rotor outer diameter is fixed. When the rotor outer diameter and the slot size remain unchanged, the core may be saturated with the change in the stator outer

diameter. In order to avoid this situation, the optimization range of stator outer diameter is limited between 840 mm and 880 mm. To obtain a suitable back EMF, the variation range of the core length is set from 900 mm to 940 mm. Due to the constraints of the stator and rotor assembly, the mechanical air gap length should not be too small, and if the air gap length is too large, then the magnetic field of the air gap will be small, which does not meet the requirements. Therefore, the variation range of the air gap length is limited to 2–5 mm. If the number of conductors per slot is too small, then it will not meet the efficiency requirements. On the other hand, if the number of conductors per slot is too large, then it will lead to an increased thermal load. Therefore, the number of conductors per slot is set to vary between 8, 10, and 12.

**Table 2.** Optimized design parameters and variation range.

Parameters	Range
Pole arc coefficient $\alpha_p$	[0.65, 0.95]
PM thickness $TH_p$ (mm)	[10, 15]
Stator outer diameter $D_s$ (mm)	[840, 880]
Core length $L_{ef}$ (mm)	[900, 940]
Number of conductors per slot N	[8, 10, 12]
Air gap length $\delta$ (mm)	[2, 5]

### 3.2. Response-Surface Analysis

The response-surface optimization method takes into account the random error of the experiment, and a reasonable experimental design method is used to obtain certain data through experiments. The response-surface method generally uses a second-order polynomial mathematical model to construct a response-surface model, and its specific expression is as follows [18]:

$$y(x) = \beta_0 + \sum_{i=1}^n \beta_i x_i + \sum_{i=1}^n \beta_{ii} x_i^2 + \sum_{i=1, j=1}^n \sum_{j>i}^n \beta_{ij} x_i x_j + \varepsilon \quad (1)$$

where  $\beta$  is the fit coefficient for second-order polynomial response surfaces,  $x_i$  and  $x_j$  are the design variables,  $\varepsilon$  is the error, and  $n$  is the number of design variables.

The power factor is an important parameter in motor design. A large power factor can reduce the stator current. In the optimization, it is necessary to obtain a high power factor. The power factor of a motor refers to the angle at which the voltage leads the current. In numerical terms, the power factor is the ratio of the motor's active power to the apparent power. Through a finite-element simulation, the voltage and current curves under a load operation can be obtained, and thus the phase difference of the voltage and the current can be obtained, that is, the power factor angle can be obtained. The power factor can be calculated by the cosine value of the power factor angle.

The selection of test points plays an important role in the construction of the response surface, which directly affects the accuracy of the response-surface construction. Unreasonable test points can even lead to the failure to construct the response surface. The selection of the experimental points in this paper adopts the CCD (central composite designs) method, which can obtain a lot of information about the experimental errors of the experimental variables with the fewest number of experiments. The test points are obtained by the CCD method, and simulation experiments are individually carried out for each test point. Then, the response value is fitted by Equation (1), the coefficients of the second-order polynomial mathematical model are obtained by the least-square regression analysis, and the response-surface mathematical model is finally obtained. Figure 5 shows a comparison of the predicted and experimental values for the efficiency, thermal load, power factor, core loss, copper loss and no-load back EMF. In Figure 5, the degree of the fit between the predicted value and the experimental value is relatively high, indicating that

the influence of the optimized design parameters on the performance parameters can be analyzed according to this model.

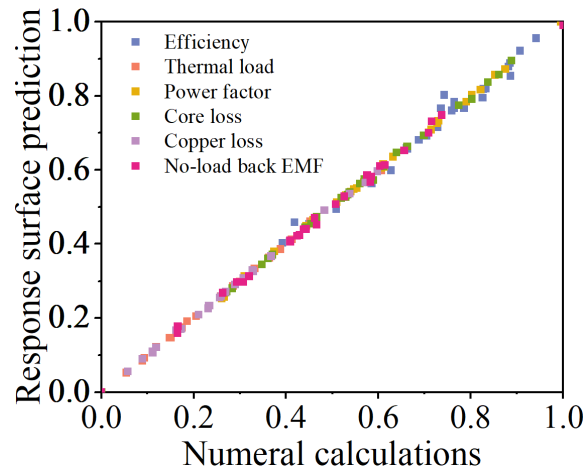


Figure 5. Fitted curve of the predicted and calculated values of the response surface.

The influence of optimized parameters on motor performance can be evaluated at the rated speed by FEA, as shown in Figures 6–9. In this analysis, the efficiency, no-load back EMF, copper loss, core loss and thermal load are obtained by the 2D FEA in a Maxwell of Ansys Workbench.

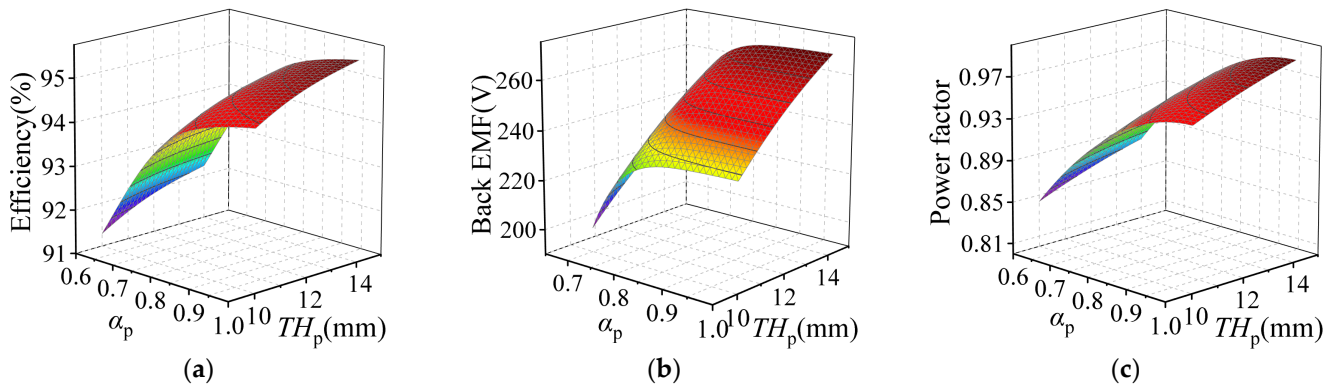


Figure 6. Response surface of pole arc coefficient and PM thickness to electromagnetic performance parameters. (a) Efficiency; (b) back EMF; (c) power factor.

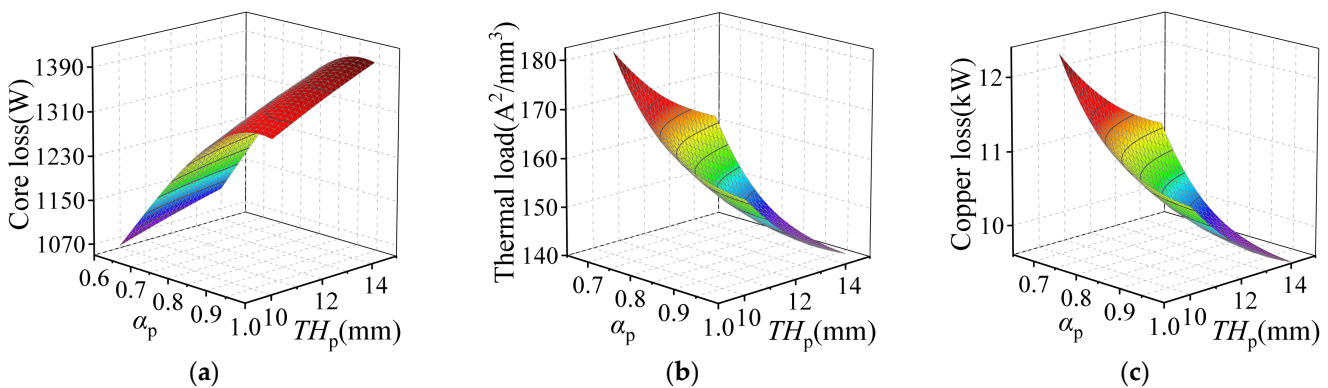
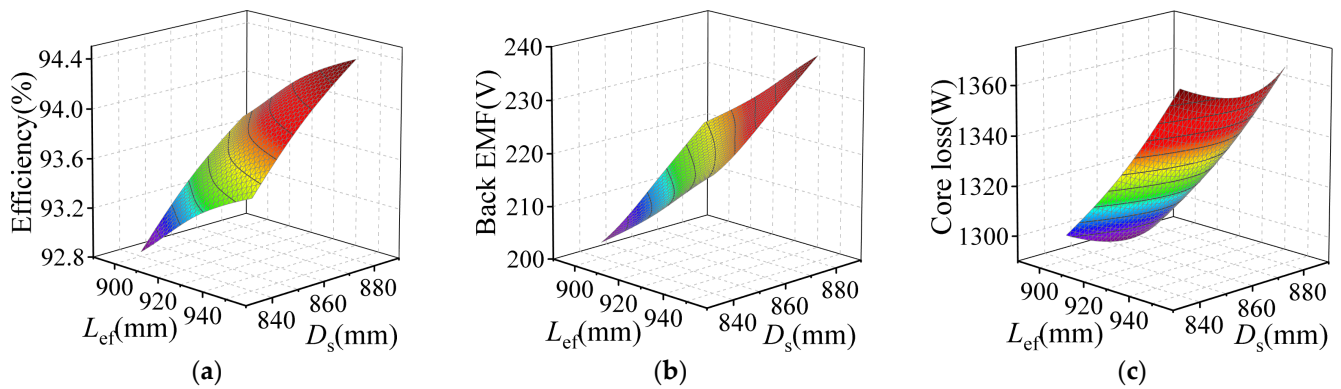
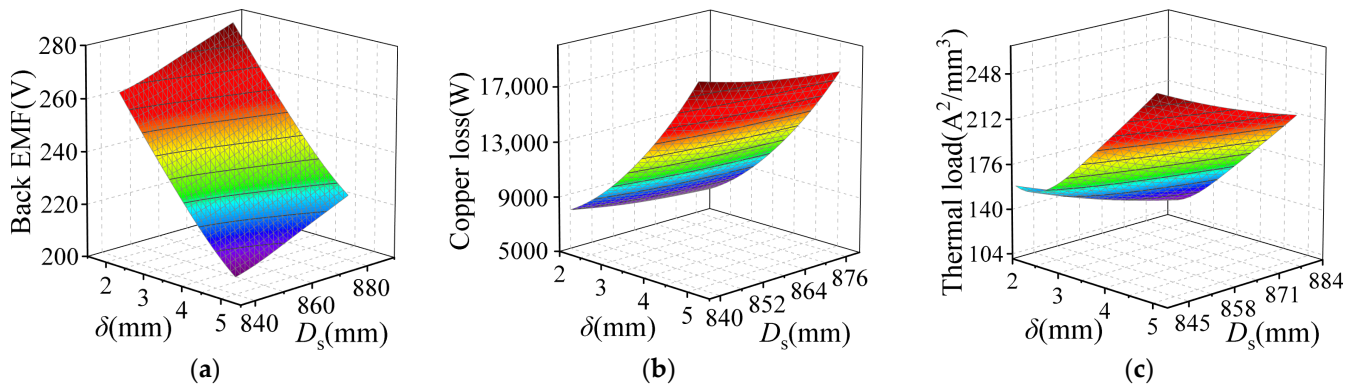


Figure 7. Response surface of pole arc coefficient and PM thickness to electromagnetic performance parameters. (a) Core loss; (b) thermal load; (c) copper loss.



**Figure 8.** Response surface of core length and stator outer diameter to electromagnetic performance parameters. (a) Efficiency; (b) back EMF; (c) core loss.



**Figure 9.** Response surface of air gap length and stator outer diameter to electromagnetic performance parameters. (a) Back EMF; (b) copper loss; (c) thermal load.

Figures 6 and 7 show the effect of the pole arc coefficient and PM thickness on the efficiency, no-load back EMF, power factor, core loss, thermal load and copper loss. In Figure 6a, as the pole arc coefficient and PM thickness increase, the efficiency increases significantly. This is due to the fact that with the increase in the pole arc coefficient and PM thickness, the magnetic flux density increases significantly, and the efficiency also increases. In Figure 6b, the no-load back EMF increases with increasing PM thickness; in addition, the no-load back EMF also increases with the pole arc coefficient, but when the pole arc coefficient is close to 0.95, the no-load back EMF decreases slightly. Figure 6c shows the effect of the pole arc coefficient and PM thickness on the power factor. The variation law of the power factor is similar to Figure 6a, with the increase in pole arc coefficient and PM thickness, the power factor gradually increases. Unfortunately, in Figure 7a, the core loss also dramatically increases with the increasing pole arc coefficient and PM thickness; this is due to eddy current losses on the motor core due to changes in the magnetic force, thereby increasing the core temperature. In Figure 7b, the thermal load decreases with the increasing pole arc coefficient and PM thickness, and in Figure 7c, the copper loss decreases with the increasing pole arc coefficient and PM thickness, which can significantly reduce the winding temperature.

The effect of the core length and stator outer diameter on the efficiency, no-load back EMF and core loss are shown in Figure 8. In Figure 8a, the efficiency increases with the increasing core length and stator outer diameter, and the stator outer diameter has a greater effect on the efficiency than the core length. In Figure 8b, the no-load back EMF is also greatly affected by the core length and the stator outer diameter. The no-load back EMF increases significantly with the increasing core length and stator outer diameter. Figure 8c shows the influence of the core length and stator outer diameter on the core loss. With the

increase in the stator outer diameter, core loss first increases and then decreases; this is because the stator outer diameter is too large or too small, which leads to the saturation of the iron core, and a larger field strength is required to generate the same amount of magnetic induction, leading to increased core loss. In addition, the core loss also increases with the increasing core length.

Figure 9 shows the effect of the air gap length and stator outer diameter on the no-load back EMF, copper loss and thermal load. In Figure 9a, the air gap length has a great influence on the no-load back EMF. As the air gap length increases, the no-load back EMF decreases significantly, which causes the current to increase. In Figure 9b, with the increase in the air gap length, the copper loss increases significantly, while with the increase in the stator outer diameter, the copper loss decreases slightly. In Figure 9c, the thermal load is affected by the air gap length and stator outer diameter in almost the same manner as the copper loss. However, as the air gap length approaches 2 mm, the thermal load tends to level off and does not decrease.

### 3.3. Sensitivity Analysis

The above analysis shows that the effects of all the optimization parameters on the electromagnetic and temperature performance are basically linear. Therefore, the Pearson correlation coefficient can be used to define the sensitivity of the optimized design parameters to the multi-objective performance parameters. The Pearson correlation coefficient is a measure of vector similarity. The output ranges from  $-1$  to  $+1$ , where 0 represents no correlation, negative values represent a negative correlation, and positive values represent a positive correlation. The formula for the Pearson correlation coefficient is as follows [19]

$$\rho_{X,Y} = \frac{\text{cov}(X,Y)}{\sigma_X\sigma_Y} = \frac{E[(X - \mu_X)(Y - \mu_Y)]}{\sigma_X\sigma_Y} \tag{2}$$

where  $\text{cov}(X, Y)$  is the covariance between  $X, Y$ ,  $\sigma_X, \sigma_Y$  are the standard deviations of  $X$  and  $Y$ , respectively, and  $\mu_X, \mu_Y$  are the expected values of  $X, Y$ , respectively.

The sensitivity of the optimized design parameters to the motor performance parameters is shown in Figure 10. Figure 10a shows the sensitivity of the optimized design parameters to the motor performance parameters when the number of conductors per slot is  $N = 8$ ; Figure 10b,c are  $N = 10$  and  $N = 12$ , respectively.

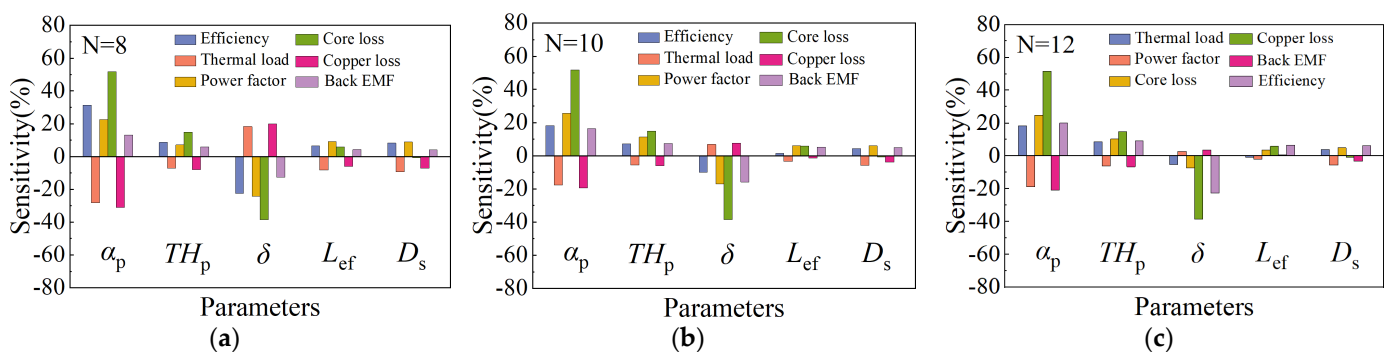


**Figure 10.** Sensitivity values for optimization parameters. (a) Conductors per slot  $N = 8$ ; (b) conductors per slot  $N = 10$ ; (c) conductors per slot  $N = 12$ .

In Figure 10, in the process of changing the number of conductors per slot among 8, 10, and 12, when  $N = 8$ , the sensitivity of the design parameters to the electromagnetic performance is the largest, and when  $N = 10$  and 12, the sensitivity of the design parameters to the electromagnetic performance decreases compared with  $N = 8$ . As shown, both the pole arc coefficient and the air gap length have a large influence on the six electromagnetic performance parameters. The PM thickness has the greatest impact on the core loss, followed by efficiency, copper loss and thermal load. The core length has a large influence

on the power factor and thermal load. The stator outer diameter also affects the thermal load, efficiency and power factor.

#### 4. Multiple Objectives Comprehensive Optimization

##### 4.1. Multi-Objective Program Design

In the multi-objective optimization design of the LSPMM, the electromagnetic efficiency and motor temperature are used as the two optimization design goals. First, the maximum efficiency is set as the optimization objective. In addition, the minimum thermal load is set as the optimization objective considering the goal of optimizing the motor temperature. For a given cooling system, both the copper loss and core loss have a great influence on the temperature distribution of the motor, but the electromagnetic simulation results of the initial LSPMM design clearly show that the copper loss is about 10 times larger than the core loss; furthermore, the stator winding is the part with the highest temperature in the motor and mainly depends on the copper loss. Therefore, in this optimization process, in order to obtain the lowest stator winding temperature, the minimum copper loss is set as an optimization objective. The objectives are defined as

$$\text{Objective : } \begin{cases} \max(\eta) \\ \min(Q_{thermal}) \\ \min(P_{copper}) \end{cases} \quad (3)$$

where  $\eta$  is the efficiency,  $Q_{thermal}$  is the thermal load, and  $P_{copper}$  is the copper loss.

The various constraints include the output torque, no-load back EMF, power factor, current density, output power and core loss.

1. Output torque: The output torque should be satisfied first in the design. For the LSPMM, its rated torque depends on the rated power and rated speed of the motor; the greater the rated power and the lower the rated speed, the greater the motor's torque. In this paper, the rated torque of the design is 34,107.1 Nm and the output torque is constrained to a minimum of 34,110 Nm.
2. No-load back EMF: The no-load back EMF is an important factor affecting the power factor. When the back EMF point is close to the voltage amplitude and the deviation is within the voltage range of  $\pm 2\%$ , the motor power factor is greater than 0.9; otherwise, the power factor is low. Therefore, to pursue a high power factor, the no-load back EMF should be limited to the vicinity of the rated voltage, which is 205 V to 220 V.
3. Power factor: The power factor is an important factor to measure the motor efficiency. The higher the power factor, the higher the motor efficiency. Therefore, the minimum power factor is set to 0.95.
4. Current density: The current density also needs to be limited. If the current density is too large, then it will increase the loss and affect the motor temperature; if it is too small, then the amount of coil material will increase. According to the traditional permanent magnet motor theory, the current density of the LSPMM is about 4–6 A/mm<sup>2</sup>.
5. Output power: The power selection of the motor should be appropriate. When the power selection is too large, the efficiency and power factor will be reduced, and when the power selection is too small, the motor will be overloaded and the lifespan will be shortened. In this optimization, the LSPMM is rated at 200 kW, so the minimum output power is limited to 200,000 W.
6. Core loss: Although the core loss is about 10 times smaller than the copper loss, the effect of the core loss on the motor temperature is not as large as that of the copper loss, but excessive core loss still affects motor performance. Therefore, the maximum core loss is set to 1500 W.

Based on the above analysis, the constraints of the LSPMM design are listed as the following:

$$\text{Constraints : } \left\{ \begin{array}{l} 34,110 \text{ Nm} \leq T_N \\ 205 \text{ V} \leq E_L \leq 220 \text{ V} \\ 0.95 \leq \varphi_p \\ 4 \text{ A/mm}^2 \leq J_C \leq 6 \text{ A/mm}^2 \\ (2E + 5) \text{ W} \leq P_{out} \\ P_{core} \leq 1500 \text{ W} \end{array} \right. \quad (4)$$

where  $T_N$  is the output torque,  $E_L$  is the no-load back EMF,  $\varphi_p$  is the power factor,  $J_C$  is the current density,  $P_{out}$  is the output power,  $P_{core}$  is the core loss.

#### 4.2. Optimization

In the optimization, the response-surface expression and the NSGA-II algorithm are obtained through the optimization module of the Ansys Workbench. During the optimization process, the objective function is evaluated by Ansys Maxwell finite-element analysis software, and the feasible region of the Pareto optimal solution can finally be obtained through calculation.

Figure 11 shows the relationship between the multi-objective performance achieved in the optimization process. In the multi-objective optimization, nearly the same thermal load is seen for multiple solutions under the same constraints, but with different efficiencies due to different design parameters. Among all the feasible solutions shown in the figure, the highest efficiency can reach 94.8%; in addition, the minimum thermal load is about  $154.5 \text{ A}^2/\text{mm}^3$ .

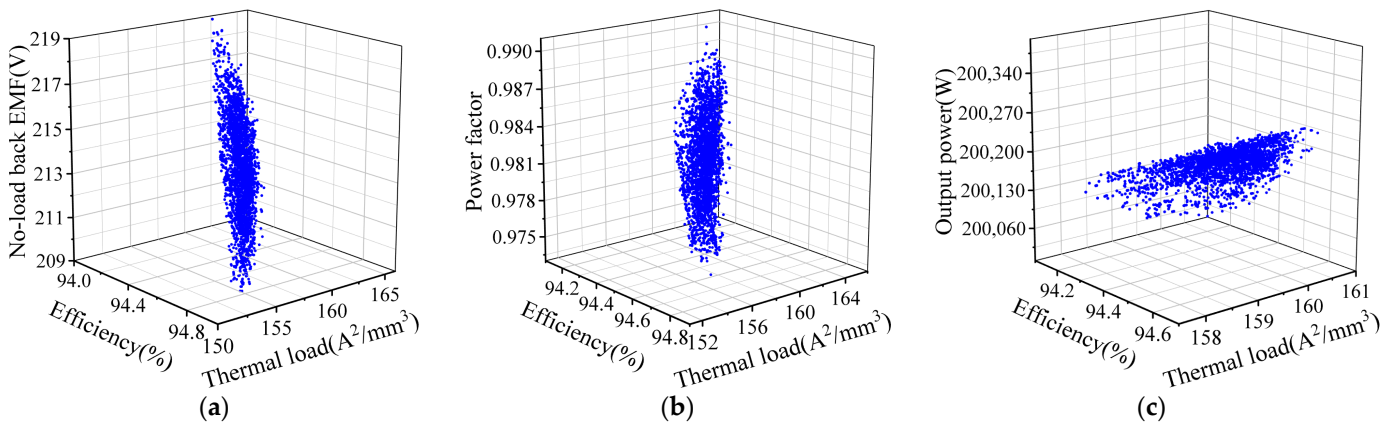


**Figure 11.** Relationship between multi-objective performances. (a) Relationship between phase back EMF, efficiency and thermal load; (b) relationship between power factor, efficiency and thermal load; (c) relationship between output power, efficiency and thermal load.

The three candidate points obtained by calculation are listed in Table 3 for comparison. In Table 3, the design parameters of the three candidate points are different, but a similar performance is obtained. The highest efficiency is 94.66% of candidate point 3, the minimum thermal load is  $156.9 \text{ A}^2/\text{mm}^3$  of candidate point 2, and the minimum copper loss is 10,684.6 W of candidate point 1.

**Table 3.** Comparison of design parameters and performance parameters of three candidate points.

	Parameters	Point 1	Point 2	Point 3
Design parameters	Pole arc coefficient	0.92	0.86	0.89
	PM thickness (mm)	13	14	14
	Stator outer diameter (mm)	878	877	877
	Core length (mm)	922	936	932
	Conductors per slot	10	10	10
	Air gap length (mm)	2.1	2	2.3
Performance	Efficiency (%)	94.61	94.65	94.66
	Thermal load ( $A^2/mm^3$ )	158.6	156.9	157.6
	Power factor	0.977	0.983	0.982
	Core loss (W)	1274.6	1258.4	1247.6
	Copper loss (W)	10,684.6	10,763	10,708.1
	Torque (Nm)	34,117.1	34,118.5	34,117.8
	No-load back EMF (V)	213	217.4	216.2
	Output power (W)	200,094	200,125	200,123

In order to maintain a reasonable temperature distribution for this motor, a water-cooling channel is provided on the stator shell, as shown in Figure 12. To compare the motor temperature distribution of these three candidates, the FEA of the temperature is conducted by motor-CAD. The turbulence model, inlet velocity, inlet temperature and the corresponding losses of the three points are set in the FEA, and the motor speed is set to 56 rpm. The temperature distribution of the motor is obtained by solving the model.

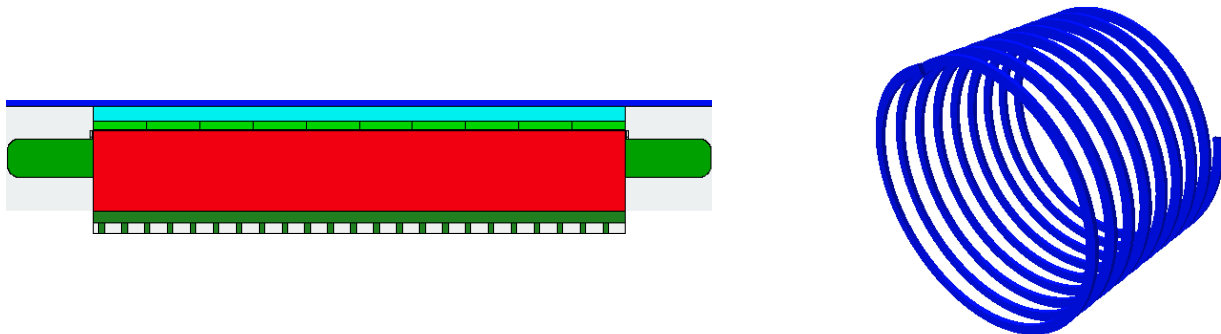
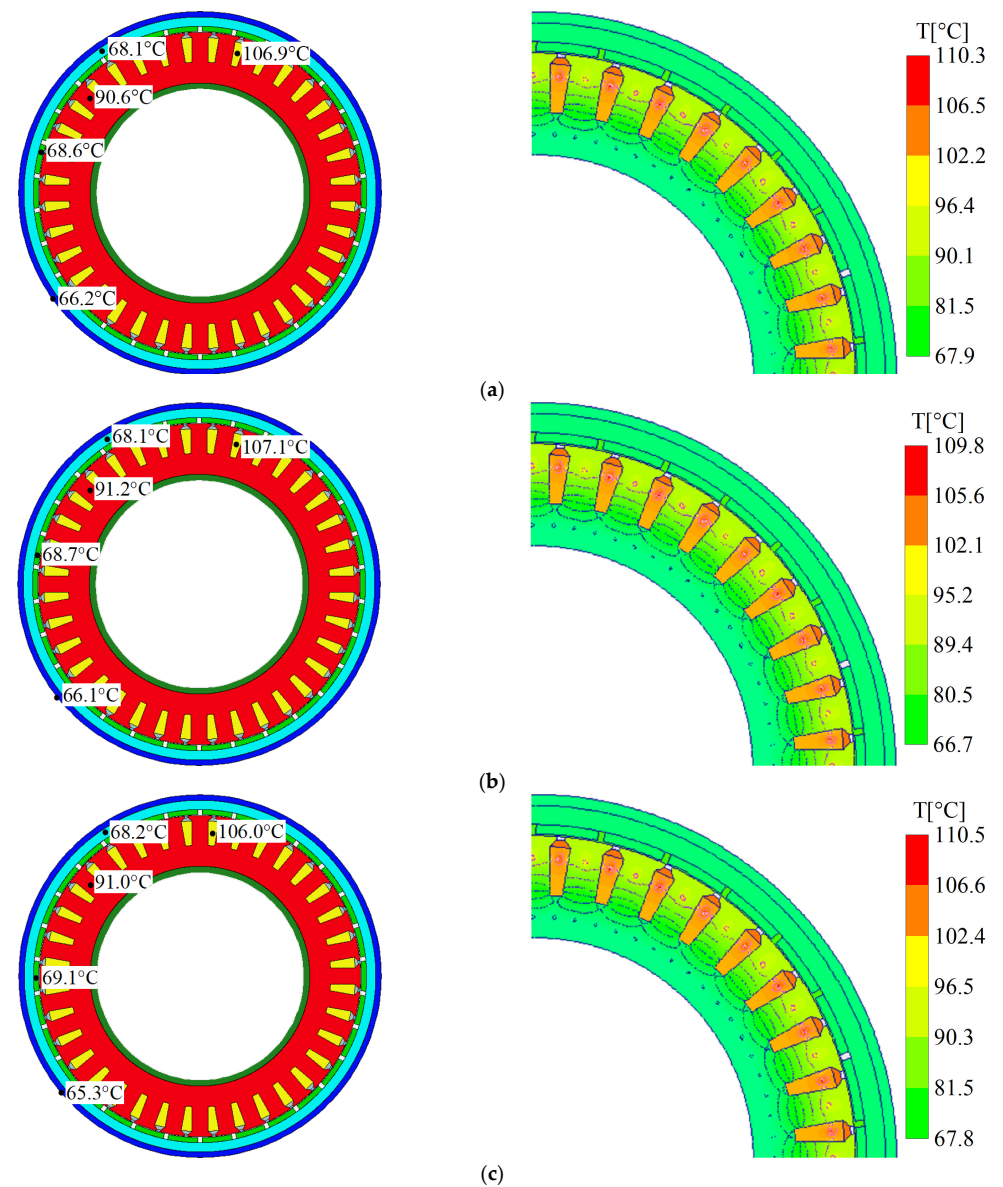
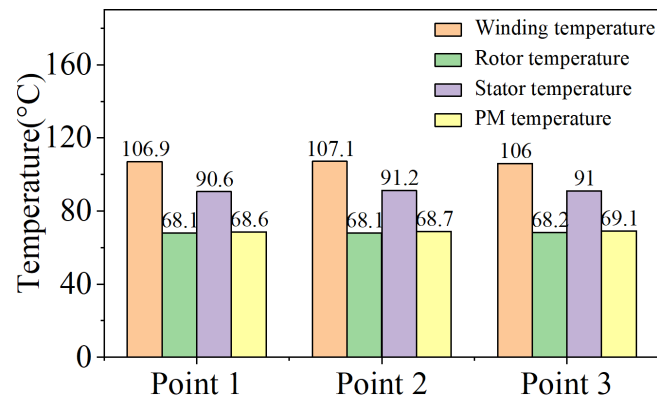
**Figure 12.** Water-cooling channel model diagram.

Figure 13 shows the simulation results of the temperature distribution of the three candidate points. As shown, the temperature in the stator area is significantly higher than that in the rotor area. This is because the stator core loss of the motor is much larger than the rotor core loss, so the stator part generates more heat and the temperature is higher. In addition, the highest temperature point of the motor appears on the motor winding, which is mainly due to the large working load of the LSPMM resulting in a large stator current, so that the copper loss generated by the motor winding is large, the thermal conductivity of the insulating material is relatively low, and the winding produces heat that is difficult to dissipate. Moreover, when the LSPMM works in the rated state, the temperature of the PM surface is low. On the one hand, the speed of the LSPMM is very low, and the PM eddy current loss generated by the motor is small. On the other hand, the inner surface of the PM is connected to the rotor core, and the thermal conductivity of the two is better; the heat generated by the PM can be quickly transferred out through the rotor core. In addition, the outer surface of the PM is in contact with the air gap, and the air flow caused by the rotor movement can take away more heat.



**Figure 13.** Temperature distribution map of candidate points. (a) Candidate point 1; (b) candidate point 2; (c) candidate point 3.

Figure 14 shows the temperature comparison of the three candidate points. As shown, the winding temperature, rotor temperature, stator temperature and magnet temperature are compared, respectively. In terms of the winding temperature, point 1 is similar to point 2, and is higher than point 3. At the same time, the lowest temperature is 106 °C in point 3, and the highest temperature is 107.1 °C in point 2. In terms of the stator temperature, the minimum temperature at point 1 is 90.6 °C, while the maximum temperature at point 2 is 91.2 °C. In addition, the rotor temperature and PM temperature are almost the same in the three points.



**Figure 14.** Comparison diagram of winding temperature, rotor temperature, stator temperature and PM temperature of candidate points.

### 5. Performance Evaluation

Through the above multi-objective optimization analysis and combined with the actual situation, candidate point 3 is determined as the final design scheme. The comparison between the initial and optimized schemes is listed in Table 4. In Table 4, the optimized design has a larger pole arc coefficient, PM thickness and stator outer diameter, and it has a smaller number of conductors per slot and a smaller air gap length. The core length does not change much from the initial design considering the actual machining and installation process.

**Table 4.** Initial and optimized parameters.

Parameters	Initial	Optimization
Pole arc coefficient $\alpha_p$	0.7	0.89
PM thickness $TH_p$ (mm)	11	14
Stator outer diameter $D_s$ (mm)	863	877
Core length $L_{ef}$ (mm)	930	932
Conductors per slot N	12	10
Air gap length $\delta$ (mm)	3	2.3

The comparison of the initial and optimized electromagnetic performance can be obtained by finite-element analysis. The comparison of the no-load back EMF, output torque, core loss and copper loss is shown in Figure 15.

In Figure 15a, the amplitude of the no-load back EMF of the optimized scheme is basically the same as that of the initial scheme, while the no-load back EMF waveform of the optimized motor scheme is more sinusoidal than that of the initial scheme. In Figure 15b, the output torque of the initial and optimized schemes is almost the same, which meets the design requirements. In Figure 15c, compared with the initial scheme, the optimized core loss is approximately doubled. Since the pole arc coefficient and PM thickness in the optimized scheme are increased compared with the initial scheme, the magnetic flux density of the optimized motor increases, resulting in an increase in the core loss. In Figure 15d, the copper loss is reduced from the initial 15,572.8 W to the optimized 10,708.1 W. In the optimization process considering the motor temperature distribution, the highest temperature point of the LSPMM appears on the stator winding, and the copper loss has a direct impact on the winding temperature. In addition, due to the low-speed and high-torque characteristics of the LSPMM, the copper loss is about 10 times larger than the core loss. Therefore, in the optimization process, the minimum copper loss is set as the main goal, while a quantitative increase in the core loss is acceptable.

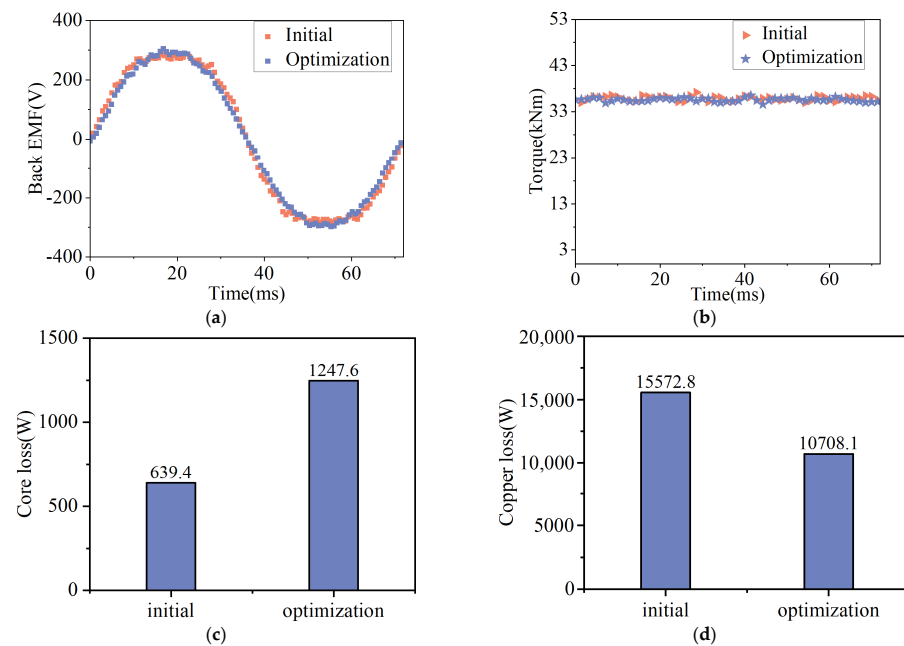


**Figure 15.** Performance comparison of initial and optimization. (a) Comparison of initial and optimized back EMF; (b) comparison of initial and optimized torque; (c) comparison of initial and optimized core loss; (d) comparison of initial and optimized copper loss.

Figure 16 shows a comparison of the initial and optimized temperature distributions. In Figure 16, the optimized maximum winding temperature is 106 °C, which is 17.9 °C lower than the maximum winding temperature before optimization.

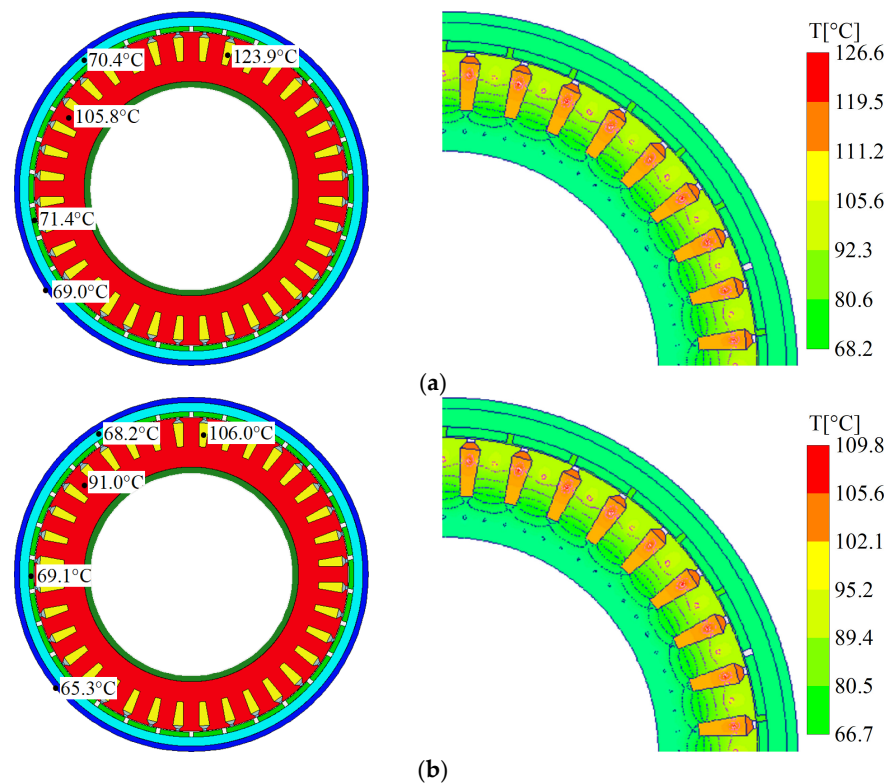


**Figure 16.** Temperature distribution map of initial and optimization. (a) Temperature distribution map of the initial; (b) temperature distribution map of the optimization.

The performance comparison of the final initial scheme and the optimized scheme is listed in Table 5. In Table 5, compared with the initial scheme, the efficiency of the optimized scheme increased by 2.04%, and the thermal load and copper loss decreased by  $76.1 \text{ A}^2/\text{mm}^3$  and  $4864.7 \text{ W}$ , respectively. In addition, the power factor also increased from 0.910 to 0.982, the torque ripple decreased by 0.4%, and the air gap flux density increased from 0.84 T to 0.92 T.

**Table 5.** Comparison of initial and optimized performance.

Parameters	Initial	Optimization
Efficiency (%)	92.62	94.66
Thermal load ( $\text{A}^2/\text{mm}^3$ )	233.7	157.6
Power factor	0.910	0.982
Core loss (W)	639.6	1247.6
Copper loss (W)	15,572.8	10,708.1
Torque (Nm)	34,110.7	34,117.8
No-load back EMF (V)	215.2	216.2
Current density ( $\text{A}/\text{mm}^2$ )	4.074	3.690
Torque ripple (%)	7.2	6.8
Air gap flux density (T)	0.84	0.92

## 6. Experimental Tests

According to the multi-objective optimization design, a 22 kW, 380 V, 56 rpm LSPMM prototype is manufactured. The prototype adopts a PM with a thickness of 14 mm and a pole arc coefficient of 0.89. The stator adopts a round copper wire with double-layer winding.

For the experimental evaluation of the overall performance of the LSPMM prototype, an experimental test platform is built, as shown in Figure 17. In the test platform, the prototype is driven by a variable frequency power converter. To obtain the voltage and current values, the voltage and current sensors are employed.



**Figure 17.** Prototype and experimental platform.

The power factor of the prototype can be directly measured by the power analyzer. The load power can be obtained from the test platform, as shown in Figure 17. The load is connected to an existing DC motor, and thus the load power is equal to the output power of the DC motor. The efficiency of the DC motor can be obtained from the manufacturer, and the input power of the DC motor can be obtained by calculation under the premise that the efficiency and output power of the DC motor are known. The prototype and the DC motor are connected by a belt, so the input power of the DC motor is equal to the output power of the prototype. In addition, the input power of the prototype can be obtained through the control system in the test platform. Therefore, the efficiency of the prototype can be obtained by the obtained input and output power of the prototype.

At the rated speed, the voltage of the prototype measured by the test platform is 378 V, which is in good agreement. Under the rated load, the measured power factor is

0.98, which is consistent with the calculation results of 0.982. In addition, the efficiency of the prototype is 94.2%, which is slightly lower than the calculated result of 94.66%. To evaluate the machine temperature, the winding temperature is measured by Pt100 resistance temperature detectors in the end windings. Table 6 lists the measured and calculated electromagnetic and temperature performances at the rated load. As shown, the measured temperature is only slightly higher than the calculated result. The experimental test of the prototype well proves the effectiveness of the optimization.

**Table 6.** Comparison of measured and calculated performance parameters.

Parameters	Measurement	Calculation
Power factor	0.98	0.982
Efficiency (%)	94.2	94.66
Winding temperature (°C)	109	106

## 7. Conclusions

In this paper, the multi-objective optimization of the outer rotor low-speed permanent magnet motor is carried out in order to comprehensively consider the electromagnetic performance and temperature characteristics. On the basis of the above analysis, the multi-objective optimization of electromagnetic performance is carried out in order to obtain a higher efficiency, lower thermal load and lower copper loss. Comparing the three candidate points, the final optimized scheme is obtained. Compared with the initial scheme, the efficiency is increased by 2.04%, the maximum winding temperature is reduced by 17.9 °C, the maximum stator core temperature is reduced by 14.8 °C, and the maximum rotor core temperature and the maximum PM temperature are reduced by 2.2 °C and 2.3 °C, respectively. The LSPMM prototype has been manufactured and tested experimentally, and the experimental results have confirmed the feasibility of the optimization scheme.

**Author Contributions:** Conceptualization, G.D. and Q.Z. (Qixun Zhou); Data curation, G.D. and C.H.; Formal analysis, C.H.; Funding acquisition, G.D.; Investigation, G.D. and C.H.; Methodology, G.D. and C.H.; Project administration, G.D.; Resources, G.D.; Software, C.H.; Supervision, Q.Z. (Qixun Zhou); Validation, G.D., Q.Z. (Qixun Zhou), W.G. and Q.Z. (Qizheng Zhang); Visualization, C.H.; Writing—original draft, C.H.; Writing—review & editing, G.D., C.H., W.G. and Q.Z. (Qizheng Zhang). All authors have read and agreed to the published version of the manuscript.

**Funding:** This research was funded by National Nature Science Foundation of China, grant number 52177056.

**Institutional Review Board Statement:** Not applicable.

**Informed Consent Statement:** Not applicable.

**Data Availability Statement:** Not applicable.

**Conflicts of Interest:** The authors declare no conflict of interest.

## References

1. Brock, H.; Berker, B.; Ali, E. Design of an External-Rotor Direct Drive E-Bike Switched Reluctance Motor. *IEEE Trans. Veh. Technol.* **2020**, *69*, 2552–2562.
2. Shi, Z.; Sun, X.D.; Cai, Y.F.; Tian, X.; Chen, L. Design optimisation of an outer-rotor permanent magnet synchronous hub motor for a low-speed campus patrol EV. *IET Electr. Power Appl.* **2020**, *14*, 2111–2118. [[CrossRef](#)]
3. Feng, G.H.; Yu, J.Y.; Zhang, B.Y.; Wang, B.; Sun, H.G. Study on Belt Conveyor Direct Driven by External-Rotor PMSM. *Adv. Mater. Res.* **2012**, *619*, 14–17. [[CrossRef](#)]
4. Ma, S.H. Study on the application of permanent magnet synchronous motors in underground belt conveyors. *IOP Conf. Ser. Mater. Sci. Eng.* **2017**, *283*, 012006. [[CrossRef](#)]
5. Chu, W.Q.; Zhu, Z.Q. Optimal split ratio and torque comparison of surface-mounted permanent magnet machines having inner or outer rotor. In Proceedings of the 6th IET International Conference on Power Electronics, Machines and Drives (PEMD 2012), Bristol, UK, 27–29 March 2012.

6. Li, Z.K.; Huang, X.Y.; Chen, Z.; Shi, T.N.; Yan, Y. Nonlinear Analytical Analysis of External Rotor Permanent Magnet Synchronous Motor. *IEEE Trans. Magn.* **2021**, *57*, 8204004. [[CrossRef](#)]
7. Ghaffari, A.; Rahideh, A.; Moayed, J.H.; Vahaj, A.A.; Mahmoudi, A.; Soong, W.L. 2-D Analytical Model for Outer-Rotor Consequent-Pole Brushless PM Machines. *IEEE Trans. Energy Convers.* **2019**, *34*, 2226–2234. [[CrossRef](#)]
8. Li, Z.; Feng, G.D.; Lai, C.Y.; Tian, J.B.; Li, W.L.; Narayan, C.K. Dual DC current injection-based stator winding temperature tracking for dual three-phase permanent magnet synchronous machine using Kalman filter. *IET Electr. Power Appl.* **2019**, *13*, 1726–1733. [[CrossRef](#)]
9. Sami, R.H.; Jere, K.; Jouni, I.; Antero, A. Interdependence of Demagnetization, Loading, and Temperature Rise in a Permanent-Magnet Synchronous Motor. *IEEE Trans. Magn.* **2010**, *46*, 949–953.
10. Du, G.H.; Xu, W.; Zhu, J.G.; Huang, N. Power Loss and Thermal Analysis for High-Power High-Speed Permanent Magnet Machines. *IEEE Trans. Ind. Electron.* **2020**, *67*, 2722–2733. [[CrossRef](#)]
11. Fu, Z.K.; Zhang, F.G.; Zhang, Z.Y.; Jin, S. Loss Study of Dual Stator Low Speed High Torque Synchronous Motor with Hybrid Rotor. *J. Phys. Conf. Ser.* **2021**, *1887*, 012051. [[CrossRef](#)]
12. Song, T.F.; Zhang, Z.Y.; Liu, H.J.; Hu, W.L. Multi-objective optimisation design and performance comparison of permanent magnet synchronous motor for EVs based on FEA. *IET Electr. Power Appl.* **2019**, *13*, 1157–1166. [[CrossRef](#)]
13. Hao, J.S.; Suo, S.F.; Yang, Y.Y.; Wang, Y.; Wang, W.J. Power Density Analysis and Optimization of SMPMSM Based on FEM, DE Algorithm and Response Surface Methodology. *Energies* **2019**, *12*, 3639. [[CrossRef](#)]
14. Onsal, M.; Cumhuri, B.; Demir, Y.; Yolacan, E.; Aydin, M. Rotor Design Optimization of a New Flux-Assisted Consequent Pole Spoke-Type Permanent Magnet Torque Motor for Low-Speed Applications. *IEEE Trans. Magn.* **2018**, *54*, 1–5. [[CrossRef](#)]
15. Beak, S.W.; Kim, B.T.; Kwon, B.I. Practical Optimum Design Based on Magnetic Balance and Copper Loss Minimization for a Single-Phase Line Start PM Motor. *IEEE Trans. Magn.* **2011**, *47*, 3008–3011. [[CrossRef](#)]
16. Crider, J.; Jonathan, M.; Sudhoff; Scott, D. An Inner Rotor Flux-Modulated Permanent Magnet Synchronous Machine for Low-Speed High-Torque Applications. *IEEE Trans. Energy Convers.* **2015**, *30*, 1247–1254. [[CrossRef](#)]
17. Anders, G.; Prakashraj, K. Force Density Limits in Low-Speed PM Machines Due to Temperature and Reactance. *IEEE Trans. Energy Convers.* **2004**, *19*, 518–525.
18. Rafiee, V.; Faiz, J. Robust Design of an Outer Rotor Permanent Magnet Motor Through Six-Sigma Methodology Using Response Surface Surrogate Model. *IEEE Trans. Magn.* **2019**, *55*, 1–10. [[CrossRef](#)]
19. Bianchi, N.; Degano, M.; Fornasiero, E. Sensitivity Analysis of Torque Ripple Reduction of Synchronous Reluctance and Interior PM Motors. *IEEE Trans. Ind. Appl.* **2015**, *51*, 187–195. [[CrossRef](#)]